CHALMERS
UNIVERSITY OF TECHNOLOGY

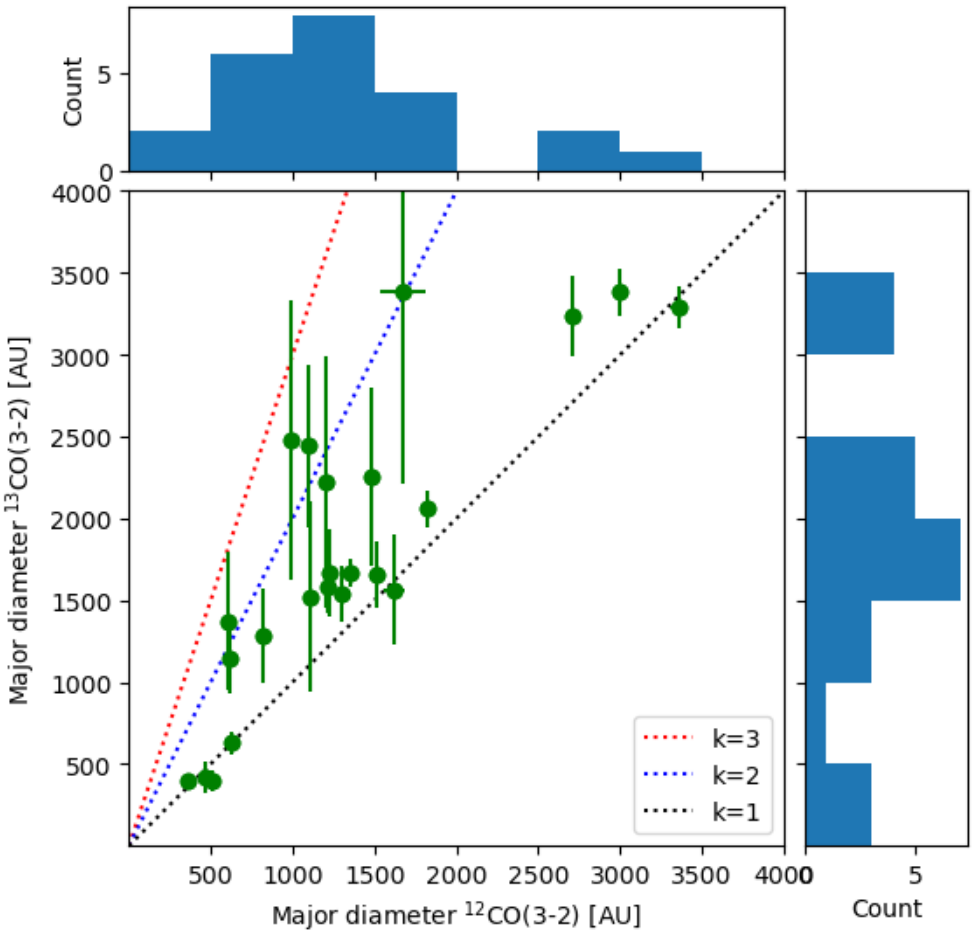

^{13}CO as a Tracer of Stellar Mass Loss

Master's thesis in Physics

MATHIAS ARVIDSSON

DEPARTMENT OF PHYSICS
CHALMERS UNIVERSITY OF TECHNOLOGY
Gothenburg, Sweden 2025
www.chalmers.se

Master's thesis 2025

^{13}CO as a Tracer of Stellar Mass Loss

MATHIAS ARVIDSSON

CHALMERS
UNIVERSITY OF TECHNOLOGY

Department of Physics
Department of Space, Earth and Environment
Chalmers University of Technology
Gothenburg, Sweden 2025

^{13}CO as a Tracer of Stellar Mass Loss
MATHIAS ARVIDSSON

Supervisor: Elvire De Beck, Department of Space, Earth and Environment
Examiner: Elvire De Beck, Department of Space, Earth and Environment

Master's Thesis 2025
Department of Space, Earth and Environment
Chalmers University of Technology
SE-412 96 Gothenburg
Telephone +46 31 772 1000

Cover: Diameter of emitting carbon monoxide gas in circumstellar envelopes of asymptotic giant branch stars.

Typeset in LaTeX
Gothenburg, Sweden 2025

^{13}CO as a Tracer of Stellar Mass Loss
MATHIAS ARVIDSSON
Department of Physics
Chalmers University of Technology

Abstract

During the Asymptotic Giant Branch (AGB) phase, stars lose a significant amount of their mass, forming a large circumstellar envelope (CSE) around the star. Modelling this outflow of gas and dust is important for understanding both the inner workings of the star, the properties of the resulting stellar remnant, and for characterising the chemical enrichment of the interstellar medium. One step to improve current mass-loss models is to constrain them using observations of the emitting gas present in the CSE. The aim of this thesis is to investigate the size and shape of the emitting CO gas in the CSEs of a sample of 61 AGB stars with varying stellar and circumstellar properties. This was done by studying the rotational molecular line emissions from ^{12}CO J=3→2 and ^{13}CO J=3→2 of all 61 sources using interferometry data collected with the Atacama Large Millimeter/Submillimeter Array (ALMA). To avoid impact of image reconstruction on the results, the observed line emissions were fit with a two-dimensional gaussian distribution in the visibility domain. From these fits the size and shape of the emitting region was determined.

^{13}CO J=3→2 emission was detected in 32 of the 61 stars investigated. Values of the major axis, minor axis, and axis ratio of the emitting regions of both molecular lines are reported for all sources when present. In general, the ^{13}CO emitting region was found to be larger than its ^{12}CO counterpart, in line with predictions from radiative-transfer models. ^{12}CO and ^{13}CO emitting regions were found to be similarly spherical, with an average axis ratio of 0.873 ±0.003 and 0.883 ±0.022 respectively. In conclusion, the study provides good observational values on sizes of circumstellar envelopes to be used as constraints in mass-loss and radiative transfer models. However, due to the lower signal strength of ^{13}CO emission, the molecule could only be found in about half of the original sample. Consequently more stars may need to be observed in the future.

Keywords: AGB stars, circumstellar envelope, mass-loss of AGB stars, carbon monoxide.

Acknowledgements

First of all, I want to give a heartfelt thanks to my supervisor Elvire De Beck. Thank you for your continuous and patient support throughout the work of this thesis. I greatly value your insight, and it has been my privilege to learn from you these last six months.

I would also like to thank Miora Andriantsaralaza for devoting her time and helping me through any ruts during the project. Furthermore I want to thank the other members of the team: Ramlal Unnikrishnan, Mark Siebert, Wouter Vlemmings, Matthias Maercker, and any others who provided me with advice, and helped me feel welcome. A thank you also goes to my opponents August Kälvesten, and Amandus Reimer. Thank you for your honest and constructive feedback.

Lastly, I would like to extend my gratitude to the friends and family who have supported me throughout these last 5 years. I couldn't have done this without you.

Mathias Arvidsson, Gothenburg, February 2025

List of Acronyms

Below is the list of acronyms that have been used throughout this thesis listed in alphabetical order:

AGB	Asymptotic Giant Branch
ALMA	Atacama Large Millimeter/Submillimeter Array
CASA	Common Astronomy Software Application
CNO-cycle	Carbon-nitrogen-oxygen cycle
CO	Carbon Monoxide
CSE	Circumstellar Envelope
Dec	Declination
HR-diagram	Hertzprung-Russell diagram
ISM	Interstellar Medium
LM-algorithm	Levenberg-Marquart algorithm
MS	Main Sequence
pp-chain	Proton-proton chain
RA	Right Ascension
RGB	Red Giant Branch
RT	Radiative Transfer
ZAMS	Zero-Age Main Sequence

Contents

List of Figures

List of Tables

1
Introduction

Towards the end of an intermediate mass ($\sim 0.8\ M_\odot < m < 8\ M_\odot$) star's life it enters what is known as the Asymptotic Giant Branch (AGB), a phase of stellar evolution characterised by a contracting and heating carbon and oxygen core, an expanding and cooling hydrogen and helium outer envelope, and a continuous outflow of gas leaving the star. The outflow, also known as stellar wind, or mass-loss, accumulates to form a dilute, but expansive envelope around the AGB star, known as the circumstellar envelope (CSE). The properties of the CSE depend on the properties of the AGB star. As a result, key parameters of the star and its evolution can be determined by observing and modelling the CSE. The released gas also contains new elements produced in nuclear processes during the star's life, and the mass loss thus contributes to the chemical evolution of the universe. Understanding the mass loss of AGB stars is an integral part of understanding the evolution and inner processes of the star, the eventual end state of the star, as well as the chemical enrichment of the interstellar medium (ISM).

1.1 The AGB phase

The general reference for information in this chapter is "Mass-Loss of Evolved Stars" (2024) by Andriantsaralaza. M[1]. Other sources are stated explicitly.
Stars go through many evolutionary stages before reaching the AGB. A star's evolution can be understood through a Hertzprung-Russell diagram (HR-diagram), which shows how the temperature and luminosity of the star correlate. As stars evolve they follow a track through the diagram, the exact details of the evolution depend on properties such as the star's mass, and its metallicity. However all stars go through in principle the same steps, starting at the Main sequence (MS).

A brief description of the evolution up to the AGB phase is provided below, and can be seen in figure 1.1. During the MS the star converts hydrogen in its core into helium to generate energy through either the proton-proton chain (pp-chain), or the CNO-cycle (carbon-nitrogen-oxygen cycle). Once the hydrogen available in the core has been exhausted the star evolves until a new energy generating process can sustain it. The main-sequence star develops a helium core, and an outer hydrogen envelope. However without the hydrogen burning in the centre, not enough energy is generated to counteract gravity, and the core contracts. A contracting core leads to an expanding envelope, and the star grows in size which causes the surface to cool. The star enters the Red Giant Branch (RGB) phase. The Kelvin-Helmholtz

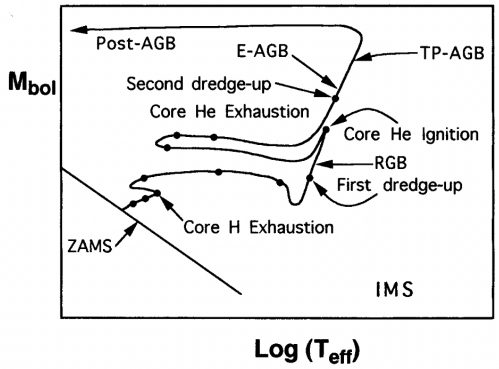

Figure 1.1: Evolutionary track of a 5 $M_\odot$ star, showing the evolution of stellar brightness versus surface temperature, going from zero-age main sequence (ZAMS), into the AGB phase, and continues into post-AGB [4].

theorem states that gravitational contraction leads to an increasing temperature, and the contracting core heats up until it becomes hot enough for helium burning to begin, which marks the end of the RGB. The star can rely on helium as fuel for a while, converting it into carbon and oxygen through a nuclear process known as the triple-alpha-process. Eventually even the helium is exhausted and the remaining carbon-oxygen core contracts while the outer hydrogen-helium envelope expands. This marks the start of the AGB phase.

Depending on the initial mass of the star, it will go through stages of burning heavier and heavier elements. However low and intermediate mass stars with masses below about 8 $M_\odot$ will not reach high enough central temperatures to ignite oxygen. Our focus in this study are on these intermediate mass stars that reach the AGB.

The structure of an AGB star

An AGB star can be described by four radial layers: the inert core, the convective envelope with a helium burning shell and a hydrogen burning shell, the dynamical atmosphere, and the circumstellar envelope.

The core of an AGB star is very dense and very hot, but it is inert, meaning that no nuclear processes are taking place. Furthermore the core contains degenerate electrons that help balance the pressure, hindering the core from collapsing. Outside the core are first a helium burning shell, a small shell in which the 3-alpha process continues, and further out is a hydrogen burning shell, where the CNO-cycle continues. The next layer is the convective envelope. It is less hot and less dense than the core but also significantly larger. Occasionally, the convective envelope reaches into the H- and He- burning shells, bringing elements such as carbon, oxygen, and more up to the surface of the star. The phenomena of the convection zone reaching far into the star and surfacing heavier elements is known as a dredge-up and it is important for the chemical diversity of the star's surface and for the contents found in the CSE. The convective envelope also pulsates, with a pulsation period depending

on the variability type of the star, but typically between 60 and 1000 days. These pulsations cause the star's radius to swell and contract. It should be noted that these pulsations are not the same as thermal pulses which happen once every about 1000 - 100 000 years. Thermal pulses however are connected to the dredge-ups, but will not be discussed in detail here.

The third layer is the atmosphere of an AGB star, and it is the outer part of its convective envelope. It is cooler and less dense than the envelope, these conditions make it possible to form molecules and dust particles. Since the star consists mostly of hydrogen atoms, the most abundant molecule formed is hydrogen gas, H_2. Two of the next most common elements brought to the atmosphere through dredge-ups are carbon and oxygen. These elements are reactive and form the second most abundant molecule in the atmosphere: carbon monoxide (CO). CO has a high bond energy and will lock up a majority of available carbon or oxygen, depending on which is least abundant. For example a star containing twice as much carbon as oxygen will bind all available oxygen to carbon, leaving half of the carbon in the atmosphere to form other molecules.

The ratio of carbon to oxygen (C/O) is therefore crucial for what other molecules can form. The ratio allows one to classify AGB stars based on their chemical type. Stars can be classified as C-type, M-type, and S-type stars. C-type stars have a carbon to oxygen ratio $C/O > 1$, meaning there is a surplus of carbon atoms. M-type stars have ratio $C/O < 1$, meaning a surplus of oxygen. S-type stars have a ratio $C/O \lesssim 1$, and differ from M-type stars in that their spectra show clear emissions from s-process elements, particularly zirconium oxide (ZrO) [6].

Dust grains are more complicated particles formed in the outer stellar atmosphere. The word dust is not implicative of a certain molecular compound but are solids containing many molecules of possibly different nature. The typical size is around 1 µm. The characteristics of the dust grains depends on what materials are available to form the grains, which depend on the chemical type of the star. Crucially, the expansion of the stellar atmosphere during pulsations cools the stellar atmosphere from about 3000 K to around 1500 K. This decrease in temperature makes it possible for dust formation to occur. Consequences of the dust formation are, firstly, that it uses up available material in the atmosphere, reducing abundances. Secondly due to the complicated molecular structure the dust grains absorb and scatter light in a large range of wavelengths. This creates a radiation pressure on the grains, and gives them outward momentum.

Nucleosynthesis

Nucleosynthesis is the process of forming new nuclei from existing elements. So far the production of helium, carbon, and oxygen have been explained through the nuclear processes of the pp-chain, CNO-cycle, and triple-α process. Other processes of nucleosynthesis involve nuclei capturing either a proton or a neutron, to either form a new element or a heavier isotope. The most important process for this project

is the formation of the isotope ^{13}C. Carbon-13 is formed through a proton capture of ^{12}C, which turns it into ^{13}N, which then beta+ decays into ^{13}C. The end product is a ^{13}C atom, and a positron and an electron-neutrino [5].

$$^{12}_{6}\mathrm{C} + ^{1}_{1}p \rightarrow ^{13}_{7}\mathrm{N} \rightarrow ^{13}_{6}\mathrm{C} + e^{+} + \nu_e \tag{1.1}$$

Elements heavier than iron can also be produced through neutron-capture processes, which are typical of AGB stars. One separates between slow neutron-capture (s-process), and rapid neutron-capture (r-process). Both include a nucleus capturing one or more neutrons before undergoing beta decay. In the r-process many neutrons are captured in a short amount of time before beta decay. The r-process is thus responsible for producing the most neutron-heavy isotopes. The s-process entails capturing one or a few neutrons before decaying. If the produced element is stable that allows time for more captures. The density of free neutrons largely determines which process will occur. The result of these processes is that a large variety of atoms are formed deep in the AGB star. When large scale convective motions bring material from deep in the star to the surface, these elements are exposed and their line emissions can be detected.

1.2 The circumstellar envelope

The circumstellar envelope is formed through a continuous outflow of gas and dust from the stellar atmosphere known as a stellar wind. The amount of mass lost can reach as high as 10^{-4} $M_\odot$ per year. The physics explaining the mass-loss mechanics are quite complicated and involve many factors coinciding to enable the mass loss. Firstly the increased size of the AGB star is imperative. The AGB star is much larger than a main sequence star. The convective envelope and atmosphere can reach over 100 $R_\odot$ in size. As a result the gravity at the outer edge of an AGB star is much weaker than compared to our sun. Secondly the pulsations of the star are important. As the envelope expands the gravitational force is weakened even further, and the outermost material is pushed, thus initiating the outflow.

However, stellar winds initiated only by pulsations reach amounts of just $\sim 10^{-12}$ $M_\odot$/ year. Another mechanism to drive the mass loss is required. The addition is radiation pressure acting on the dust grains in the atmosphere. In absorbing light, the dust grains gain both the energy and the momentum of the photon, effectively creating a force pushing the dust away from the atmosphere of the star. This additional source of momentum helps the dust overcome the gravitational pull. The dust absorbs far more radiation than the gas, and is accelerated outward, dragging gas along through collisions. The phenomenon is called dust driven wind.

As the dust pushes gas molecules out over many years, a large structure surrounding the AGB is accumulated. This is known as the circumstellar envelope, and its contents will be largely the gas and dust formed in the atmosphere. The majority of the mass will be in the form of the abundant hydrogen gas, as well as carbon monoxide, CO. The complicated dust grains make up only about $0.1\% - 1\%$ of the

total mass content. Furthermore the CSE will contain a rich variety of molecules depending on the chemical type of the AGB star at its centre.

At the outer edge of the CSE, interstellar radiation can break apart molecules through photodissociation, and form even more different types of molecules. Photodissociation is simply the absorption of a photon to break the bond between two atoms, and requires the photon energy to surpass or equal the bond energy. Molecules with stronger bonds are tougher to break apart, and last further out into the CSE as a result. CO molecules have some of the strongest bonds, and fill a large part of the CSE. This makes CO an optimal molecule to study the properties of the CSE. Another important factor in determining how far out into the envelope a molecule survives is its abundance. As we have established, CO is the second most abundant molecule ejected through stellar winds.

H_2 might be the most abundant molecule, however, due to its symmetric molecular structure the gas molecules in their unexcited state lack a permanent electric dipole moment, and as such are difficult to observe [7]. CO molecules on the other hand, are asymmetrical, and have a net positive spin. This small dipole moment makes the molecules easily excited from collisions with dust and other gas particles. The excited molecules then emit line emissions corresponding to the energy difference between the rotational energy levels. These line emissions are relatively easy to detect and also verify the existence of the molecules. The transitions of most importance to this paper are the rotational transitions ^{12}CO(J=3 $\rightarrow$ 2) and ^{13}CO (J=3 $\rightarrow$ 2), with corresponding rest frequencies $f_{^{13}\mathrm{CO}(3-2)} = 330.588\,\mathrm{GHz}$, and $f_{^{12}\mathrm{CO}(3-2)} = 345.796\,\mathrm{GHz}$ [8, 9]. Furthermore ^{12}CO and ^{13}CO have different bond strengths, with ^{12}CO being somewhat stronger.

The continuous mass loss forming the CSE is often assumed to be isotropic, leading to a spherically symmetric CSE. This common assumption is called the standard CSE model. However, some AGB stars have been found to possess asymmetrical circumstellar envelopes [3]. Measuring the actual shape is important for improving models of circumstellar envelopes. Another important property of the CSE is its size, which is used when calculating the mass-loss. Accurate measurements of the size and shape of the CSE is crucial when creating accurate models of mass-loss.

Historically, modelling the CSE has been challenging due to large uncertainties in the sizes, shapes, and distances measured to the stars. The DEATHSTAR project was launched to rectify this [2].

1.3 The DEATHSTAR project

The DEATHSTAR project was launched in 2020 with the goal of improving mass-loss rate estimates by accurately measuring sizes and asymmetries of CO envelopes surrounding a sample of Asymptotic Giant Branch stars [2]. For a long time sizes of circumstellar envelopes have been a large source of uncertainty in mass-loss models. With the opening of the radio interferometer Atacama Large Millimeter/Sub-

millimeter Array (ALMA), enabling more precise measurements, the updated sizes found through the DEATHSTAR project can be used to constrain mass-loss models.

The first papers published in the DEATHSTAR project reported the sizes and asymmetries of 42 and 27 CSEs respectively [2, 3]. This was accomplished by observing the ^{12}CO rotational line emissions J = 2 → 1 and J = 3 → 2 from a large sample of AGB stars. CO is an ideal molecule to observe because it is present in the CSE of all AGB stars, it is one of the most abundant molecules, and it has clear line emissions that are easily detected and identified [1].

While the previous studies found the sizes and asymmetries of CSEs in ^{12}CO, which does constitute a majority of the carbon monoxide, a complete picture also needs to account for the second most common isotopologue, ^{13}CO. Furthermore since ^{12}CO and ^{13}CO share many properties, it provides an interesting study of how their differences come into effect. Specifically the bond energy of the two molecules differ by a small amount and their abundances are significantly different. One expects this to result in a different abundance profile over the radius of the CSE because of the effects of photodissociation. Measuring the sizes and shapes of ^{13}CO emission regions can therefore not only help complete the understanding of CO-outflow, but also help constrain photodissociation models, and help in improving radiative transfer (RT) models.

1.4 Aim

This project aims to further improve the understanding of stellar winds by studying the sizes of the ^{13}CO$(3-2)$ emitting region in the circumstellar envelope of AGB stars, and will compare the sizes and structures to those found for ^{12}CO$(3-2)$ in the same stars. The sizes for ^{13}CO will hopefully provide further constraints on theoretical mass-loss, and radiative transfer models, as well as enable more detailed photodissociation modelling by comparing the distributions of ^{12}CO and ^{13}CO in the CSE.

As a verification, the project will firstly aim to reproduce some observational results previously found for ^{12}CO, and then apply similar methods to find the sizes of ^{13}CO. This will serve as a sanity check and will add validity to new findings and provide an opportunity to improve on previous results.

The project will thus contribute to an improved picture of the CSE structure in ^{13}CO, provide a direct comparison to the more well studied CSE structure in ^{12}CO, and also provide insight into the excitation of CO gas in the envelope. Hopefully the results presented in this paper can be used as constraints in models of mass-loss, and radiative transfer.

1.5 Limitations and scope

The sample of stars studied in DEATHSTAR consists of about 180 AGB stars. This project studies a subset of the full sample and includes 61 out of the 68 stars treated in the first two DEATHSTAR papers. In summary, the sample is made up of 23 C-type stars, 23 M-type stars, and 15 S-type stars. The chosen sample provides a good variety of initial masses, variabilities, chemical types, expansion velocities and other relevant stellar parameters. The sample is thought to be a good representation of mass-losing AGB stars in the galaxy [2].

For all 61 stars investigated the size and structure of the ^{12}CO and ^{13}CO emitting regions was found when available. No other line transitions are considered. Furthermore the standard CSE model will be used in this project. The standard CSE model assumes the envelope to be spherically symmetric, so that the distribution of gas and dust particles surrounding the star is isotropic, and temperature and density only depend on the radius from the centre of the star. This is assumed to be generated from a constant mass-loss rate, with a velocity that only changes within a brief acceleration zone close to the star's atmosphere.

1.6 Outline

Chapter 2 presents the methods used to find the size of CSE, as well as information on how to manipulate interferometry data, and how this data should be interpreted. Sizes and shapes of the entire studied sample are presented and discussed in chapter 3. Furthermore the structure of three individual stars are presented and discussed more deeply, providing insight into the limitations of the study, and how ^{12}CO and ^{13}CO behave differently in the CSE. Lastly chapter 4 provides a brief conclusion, summarising the previous chapters.

2

Methods

2.1 Introduction to interferometry and ALMA

The data was collected with the radio interferometer Atacama Large Millimeter/-Submillimeter Array (ALMA). A radio interferometer is a collection of many smaller telescopes all measuring the same object at the same time. This can be compared to the alternative technology of single-dish telescopes, which as the name suggests is only a single parabola. The principle behind the interferometer is that by strategically spreading out many smaller telescopes, the signal from the target source will reach each telescope at a slightly different time. This difference in time causes a phase shift which provides spatial information about the target that cannot be achieved using single-dish telescopes. Furthermore the largest distance between two array elements, called the baseline, determines the resolution of the interferometer. It can achieve a much greater resolution than that of a single dish telescope which is limited by the size of the parabola [11].

The data for the project was downloaded directly from the ALMA science archive [12]. The original datasets captured for the DEATHSTAR project contained data from frequency bands B6 and B7 [2]. The lines for both ^{12}CO(3-2), $f = 345.796$ GHz and ^{13}CO(3-2), $f = 330.588$ GHz were found in B7, and since this data had already been captured it could be used for this study.

The interferometer measures the amplitude and phase of signals between pairs of antennas as a function of frequency and time. The measurements are then cross-correlated to produce the fundamental observable known as a visibility. The properties of the visibility depends on the locations of the telescopes of the array, where the source is located in the sky, and the wavelengths being observed. The visibility is a complex function containing information about the amplitude and phase of the emission at a range of frequencies. Visibilities are usually expressed in a coordinate system called the uv-plane, where the coordinates u and v are spatial frequencies along the east-west and north-south directions respectively [1].

To use the data, one first has to calibrate the visibilities, which corrects for possible atmospheric disturbances, and accounts for effects from the equipment. Then to image the data a Fourier transform is applied, followed by a deconvolution [1]. These processes will not be covered here. In this study the standard ALMA calibration procedure that comes delivered with the data was used. Calibration is performed by

running a script delivered along with the datasets with the correct pipeline version of CASA. The pipeline can be seen as an instruction on how to calibrate the data based on how the system was operated at the time of measuring.

The work was done in CASA - Common Astronomy Software Application, which is similar to a python environment launched in the terminal. CASA has been specifically developed to work with ALMA data, and as such comes with great support and many usable functions that can be applied directly to ALMA data sets.

While it is possible to image the data first and then perform fitting in the spatial domain, there are advantages to fitting directly in the uv-plane. Image reconstruction is done through some model of the observed structure and necessarily introduces assumptions that might interfere with the end result. The image ends up being a non-unique representation of the visibility information. By fitting in the uv-plane we avoid deriving results from reconstructed images that might be affected by these issues.

2.2 Interpreting observations of the CSE

The CSE is observed at a range of frequencies, and after calibration we obtain an image at every frequency. In fact the final dataset is a three-dimensional object called a data cube. This dataset has two spatial axes giving an image of the sky plane, and one frequency axis. This cube does not give a spatial cross-section of the CSE, since only two of its axes are positions. The third axis is a frequency and encodes the doppler shift of the emissions in the CSE in relation to the observer.

The star at the centre moves, relative to the observer, with the so called systemic velocity, and the gas in the CSE is ejected from the star at the expansion velocity. A spherical and isotropically expanding cloud of gas has the same expansion velocity in all directions. However, some gas will be travelling towards the observer, some will be travelling away, and some will travel in a direction orthogonal to the line of sight. The different resulting projected velocities lead to doppler shifts in the line emissions and let us measure emission from different regions of the CSE, as illustrated in figure 2.1. At each frequency in the data cube the observer sees the gas with the corresponding velocity component parallel to the line of sight in a spherical distribution. Spatially this translates to cones at different angles throughout the CSE. No matter the frequency, when the conical emission region is projected into a plane, a circular emission should be detected.

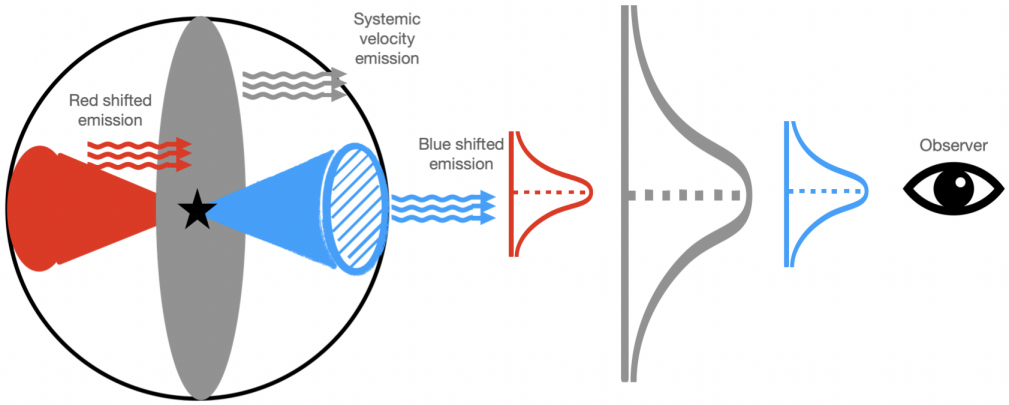

Figure 2.1: Emission from gas moving with different relative velocities to the observer are separated due to doppler shifts. Each velocity gives an emission profile to be fitted. Spatially each velocity corresponds to a cone in the CSE, where the velocity component in the direction of the observer is the same.

Next we consider the effects of radiative transfer on the observed emission. While we observe emissions from the entire CSE, depending on the optical properties of the material not all of the light emitted reaches us. Specifically a species of molecules can absorb the same frequencies they emit. If a material is very dense, the chance of emission being reabsorbed is high. The same emission is then re-emitted in a random direction. This can cause emission from the inner parts of the CSE to get blocked by the outer gas, and the only emission that reaches us is from the outermost layers. This type of material is called optically thick, or is said to have a high optical depth [11], meaning we cannot see far into the CSE. At the same time, a low density gas has a low chance of absorbing its own emissions, light from deep inside the CSE is then more likely to escape. This type of material is called optically thin. Considering that ^{12}CO is much more abundant than ^{13}CO we expect effects of optical depth to be more prominent in ^{12}CO emissions.

Even though the rest frequency for the CO lines is constant, the actual frequency at which the line is observed changes between sources. This is because each star moves with its own unique systemic velocity and emission lines are doppler shifted accordingly. The exact frequencies to be fitted were therefore identified manually, and was done by searching in the vicinity of the rest frequencies.

The data quality of ^{12}CO was superior to that of ^{13}CO, which in many cases proved rather noisy. This discrepancy is due mainly to abundance differences. More ^{12}CO gas leads to more emitting molecules, and stronger signals. For ^{13}CO the data quality was varied. Several stars showed strong ^{13}CO emission, while for some sources no line was detected. A strong line makes fitting easier and introduces less errors and is always preferred.

2.3 Uvmultifit

The main tool used to characterise the size, shape and behaviour across velocity space of circumstellar envelopes was uvmultifit, a procedure that can be run using CASA. The sources for this section are [13] and [14].

Assuming a standard CSE spherical distribution of gas around the star, the measured emission will approximately take the shape of a 2D gaussian centred on the stellar position. As such we expect to retrieve a 2D gaussian profile at every velocity for which we measure emission. The position and size of the gaussian fit in turn inform us about the location, size and symmetry of the emitting CO gas.

With uvmultifit a 2D gaussian is fitted to the visibilities at a certain velocity, and this is done for all specified velocities in the emission range. The fit gives values and errors for the following 6 variables: right ascension (RA) offset ["], declination (dec) offset ["], flux [Jy], major axis ["], axis ratio [1], and position angle [degrees]. A short explanation of each variable is as follows: RA and Dec are positions on the sky, corresponding to the coordinates of the emission region's centre. Flux is the intensity of the measured emission, corresponding to the peak of the gaussian. Position angle is a variable encoding how the gaussian is angled. The major axis is the angular size along the largest diameter of the emitting region. Similarly one can define the minor axis as the axis perpendicular to the major axis. The axis ratio is given by the ratio of the minor and major axes.

Uvmultifit uses the Levenberg-Marquart algorithm (LM-algorithm), which is a common general algorithm for solving non-linear least-squares problems. The algorithm is a combination of the Gauss-Newton algorithm and gradient descent. Similar to other iterative optimization procedures, the algorithm finds a local minimum, but does not always find the global minimum, meaning it always finds a solution, but not necessarily the best solution. Consequently the results must be examined critically, and one should make sure the result is physically reasonable.

Finding the optimal solution, therefore, requires a good choice of initial conditions. The instructions used by uvmultifit in this project are described below. The model was selected to be gaussian. The number of iterations per channel was set to the default of 20. The initial conditions and boundaries for the 6 variables RA, dec, flux, major axis, axis ratio, and position angle were specified as in table 2.1.

Only the major axis initial value was altered between stars. Using the same value for all CSEs makes little sense, as they are intrinsically of different sizes and located at different distances from the observer. The approach used in deciding initial values was to start from major axis values of $^{12}CO(3-2)$ reported in Ramstedt et. al (2020), and Andriantsaralaza et. al (2021) in the first DEATHSTAR papers [2, 3]. For $^{12}CO(3-2)$ this generally gave very high quality fits, but for $^{13}CO(3-2)$ the initial value had to be modified. Using the $^{12}CO(3-2)$ major axis value as a starting point, a few fits were done with both smaller and larger initial values, and the best

fit was chosen by eye.

The stars in our sample have different intrinsic parameters such as mass-loss rates, CO envelope sizes, and are in addition to this located at different distances. The uvmultifit results for major axis are an angular size measurement of the emitting regions. To compare results among our sample we should convert to a physical size scale. This is done by scaling for the distance, and by converting units. To get the major diameter, D, of the CSE in astronomical units [AU], one multiplies the major axis θ_{maj}, in arcseconds, with the distance to the star, d, in parsec, as in equation 2.1. Distances used to calculate sizes were taken from Andriantsaralaza et al. (2022) [15].

$$D[\mathrm{AU}] = \theta_{\mathrm{maj}}[''] \cdot d[\mathrm{pc}]. \tag{2.1}$$

Table 2.1: The variables, their initial values and boundaries used by uvmultifit when fitting a 2D Gaussian to the visibility data. The initial value for major axis was varied between stars based on previously reported values.

Variables:	RA	Dec	Flux	Major Axis	Axis ratio	Position Angle
Initial Values:	0.0	0.0	3.0	From DEATHSTAR	0.99	0.0
Boundaries:	[-2, 2]	[-2, 2]	[0, 80]	[0.1, 10]	[0.5, 1.0]	[-90, 90]

2.4 Structure plots

With the 2D Gaussian fit completed, the value of the variables RA, Dec, Major axis, and Minor axis were plotted over velocity in so called structure plots, of which an example is shown in figure 2.2. A few structure plots are discussed in detail in Chapter 3.3. The plots were also used to judge how well the results of the fit seem to agree with a spherical emitting region.

The x-axis of a structure plot shows the velocities covered by the CSE. The unit on the x-axis is velocity [km/s] in the local standard of rest frame, v_{lsr}. The local standard of rest is a frame of reference following the mean velocity of sun and surrounding materials in the milky way, and it is in this frame that each star moves with its systemic velocity. The y-axis has the unit of arcsec, an angular size, meaning how large something appears on the sky when observed from earth. Lastly the four lines are the values of major axis (blue), minor axis (yellow), RA (red) and Dec (green). According to spherical models of the CSE, the value of the major axis is expected to peak at the systemic velocity.

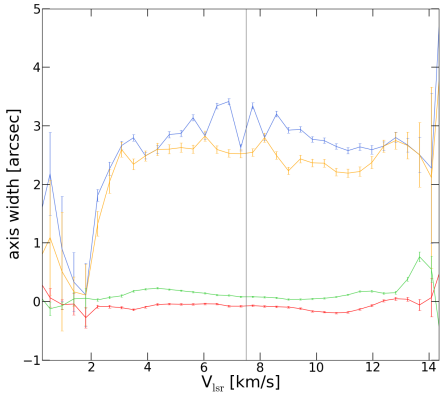

Figure 2.2: Structure plot of $^{12}CO(3-2)$ gas in the CSE of the star SU Vel. The figure shows how the variables RA (red), Dec (green), major axis (blue), and minor axis (yellow) vary with velocity. The plot is centred around the systemic velocity of the star indicated by the vertical grey line.

The values reported in table 3.1 and summarising figures in the results and discussion chapter for all stars were taken at the systemic velocity. Only considering the values obtained at the systemic velocity comes with some limitations. Firstly it fails to capture the variations and substructures of individual stars. Two stars can have the same axis values at the systemic velocity, and yet their structure plots might be very different. If we only considered the values at the systemic velocity the stars would look identical, when in reality they are not. Secondly, as seen in figure 2.2, some stars show significant channel-to-channel variations in axis values. In this case, the value of the major axis and minor axis match perfectly in some channels and then separate in the next. Depending on which of these options happens to be closest to the systemic velocity the resulting axis ratio can be significantly different. Even though the uncertainty at each point is very small, fluctuating values make it hard to tell whether the true axis ratio is close to one or significantly less.

3

Results and discussion

We start by presenting and discussing summarising characteristics of the entire sample, such as size and shape. We then present the structure of a select few stars and discuss interesting features in more detail.

Out of the 61 stars in the sample, $^{12}CO(3-2)$ emission was detected in all, and $^{13}CO(3-2)$ emission was detected in 32. The lower detection rate can be attributed to the lower abundance of ^{13}CO, which as a result has a weaker signal. Out of the 32 sources with $^{13}CO(3-2)$ emission, 8 had an error larger than 40% of its major axis value. These sources were deemed too noisy, and excluded from the figures summarising the size and shape of the emitting regions. The sources disqualified this way are: CW Cnc, GI Lup, IRC-10401, R For, RT Sco, SV Aqr, TT Cen, and W CMa. As a result only 24 of the original 61 stars were kept for the summarizing graphs. The structure plots of the noisy star TT Cen are discussed in further detail.

3.1 Sizes of CO envelopes

In Table 3.1 we present values of major axis and axis ratio at the systemic velocity in both molecular lines for the 32 sources. The stars are sorted alphabetically. The sizes were calculated using distances reported in Andriantsaralaza et al. (2022) [15].

To illustrate the size difference between the ^{12}CO and ^{13}CO emitting gas, the major axis of $^{13}CO(3-2)$ is plotted against the major axis of $^{12}CO(3-2)$ for the 24 sources in figure 3.1. The $^{13}CO(3-2)$ emission region is consistently larger than its $^{12}CO(3-2)$ counterpart. For most stars the size of ^{13}CO is between 1 and 2 times larger. While a few stars have ^{13}CO sizes between 2 and 3 times as large, however the error in ^{13}CO major diameter is notably large for these stars. We also note a few exceptions where the ^{12}CO envelope is just barely larger.

Table 3.1: All 32 stars where both $^{12}CO(3-2)$ and $^{13}CO(3-2)$, were detected. For each star the value of major axis, the axes ratio, and the calculated size of the emitting region is included for both CO lines.

Source	$^{12}CO(3 \rightarrow 2)$			$^{13}CO(3 \rightarrow 2)$		
	Major axis ["]	Axes ratio	D [AU]	Major axis ["]	Axes ratio	D [AU]
BK Vir	3.37 ± 0.06	0.99 ± 0.02	814 ± 15	5.32 ± 1.20	0.99 ± 0.25	1286 ± 290
CW Cnc	3.09 ± 0.12	0.96 ± 0.04	808 ± 31	4.75 ± 2.00	0.88 ± 0.37	1243 ± 424
GI Lup	2.42 ± 0.12	0.99 ± 0.10	2464 ± 122	5.10 ± 3.83	0.51 ± 0.56	5192 ± 3899
IRC-10401	2.54 ± 0.32	0.99 ± 0.09	8806 ± 1109	4.57 ± 1.88	0.99 ± 0.42	15843 ± 6517
IRC-10529	3.61 ± 0.05	1.00 ± 0.01	3354 ± 47	3.54 ± 0.14	0.84 ± 0.05	3289 ± 130
NSV 24833	2.19 ± 0.29	0.98 ± 0.13	7658 ± 1014	4.84 ± 1.75	0.99 ± 0.48	16925 ± 6119
R Crt	5.48 ± 0.07	0.80 ± 0.01	1298 ± 17	6.50 ± 0.71	0.99 ± 0.15	1539 ± 168
R For	3.70 ± 0.10	0.91 ± 0.04	1874 ± 51	7.67 ± 3.55	0.55 ± 0.32	3885 ± 1798
R Hor	4.33 ± 0.06	0.77 ± 0.03	1211 ± 17	5.66 ± 0.58	1.00 ± 0.11	7377 ± 162
R Hya	4.97 ± 0.07	0.69 ± 0.01	626 ± 9	5.00 ± 0.55	0.99 ± 0.13	1582 ± 69
R Leo	5.08 ± 0.07	0.92 ± 0.02	508 ± 7	4.00 ± 0.65	0.69 ± 0.20	400 ± 65
RR Aql	4.44 ± 0.06	0.85 ± 0.02	1823 ± 25	5.01 ± 0.28	0.90 ± 0.07	2057 ± 115
RT Sco	4.11 ± 0.09	0.87 ± 0.03	2915 ± 64	6.10 ± 3.19	0.80 ± 0.39	4327 ± 2263
RT Vir	5.41 ± 0.08	0.80 ± 0.02	1227 ± 18	7.36 ± 1.19	0.99 ± 0.20	1669 ± 270
RZ Sgr	3.14 ± 0.06	0.99 ± 0.01	1355 ± 26	3.87 ± 0.20	0.78 ± 0.06	1670 ± 86
ST Sgr	2.33 ± 0.19	0.99 ± 0.07	1676 ± 137	4.70 ± 1.63	0.56 ± 0.59	3381 ± 1173
SU Vel	2.63 ± 0.05	0.96 ± 0.02	1096 ± 21	5.86 ± 1.19	0.69 ± 0.18	2441 ± 496
SV Aqr	2.17 ± 0.17	0.91 ± 0.13	965 ± 76	5.30 ± 2.45	0.50 ± 0.50	2356 ± 1089
SW Vir	4.92 ± 0.05	0.94 ± 0.01	614 ± 6	9.20 ± 1.72	0.62 ± 0.18	1149 ± 215
T Cet	2.85 ± 0.06	0.93 ± 0.04	607 ± 13	6.45 ± 1.99	0.50 ± 0.33	1373 ± 423
TT Cen	5.45 ± 0.13	0.91 ± 0.03	6436 ± 154	5.80 ± 2.64	0.97 ± 0.35	6849 ± 3118
U Hya	5.31 ± 0.04	0.65 ± 0.01	1517 ± 11	5.80 ± 0.71	0.50 ± 0.14	1657 ± 203
U Men	3.80 ± 0.14	0.92 ± 0.04	1204 ± 44	7.01 ± 2.42	0.50 ± 0.26	2220 ± 766
UY Cet	3.30 ± 0.10	0.83 ± 0.28	1480 ± 45	5.03 ± 1.21	0.76 ± 0.22	2256 ± 543
V821 Her	3.88 ± 0.04	0.94 ± 0.01	2714 ± 28	4.63 ± 0.35	0.99 ± 0.07	3239 ± 245
W CMa	2.92 ± 0.10	1.00 ± 0.04	2267 ± 78	4.02 ± 3.30	0.83 ± 0.61	3121 ± 2562
W Hya	5.33 ± 0.10	0.86 ± 0.02	463 ± 9	4.83 ± 1.10	0.99 ± 0.19	629 ± 96
WX Psc	4.17 ± 0.07	0.91 ± 0.02	3000 ± 50	4.70 ± 0.20	0.99 ± 0.05	3381 ± 144
X TrA	3.38 ± 0.07	0.99 ± 0.03	986 ± 20	8.49 ± 2.93	0.50 ± 0.29	2477 ± 855
Y Pav	2.91 ± 0.06	0.99 ± 0.03	1108 ± 23	4.00 ± 1.53	0.99 ± 0.43	1523 ± 582
Y Scl	3.22 ± 0.13	0.64 ± 0.04	1621 ± 65	3.11 ± 0.66	0.91 ± 1.48	1566 ± 332
θ Aps	3.42 ± 0.04	0.99 ± 0.02	355 ± 4	3.79 ± 0.37	0.99 ± 0.11	394 ± 38

Considering the smaller extent of the ^{13}CO abundance profile, this result might seem counterintuitive. However, we are measuring the line emission, not the abundance profile. This means that the line excitation has to be taken into account. The gas is not necessarily excited evenly throughout the CSE. Saberi et al. (2020) showed with radiative transfer models describing the propagation of light through the CSE, that for example $^{13}CO(3-2)$ is partially emitting at larger radii than $^{12}CO(3-2)$ [16]. For the examples they showed, this radial difference can be roughly 1 to 4 times larger. This would cause the observed size of $^{13}CO(3-2)$ to indeed be larger than for $^{12}CO(3-2)$.

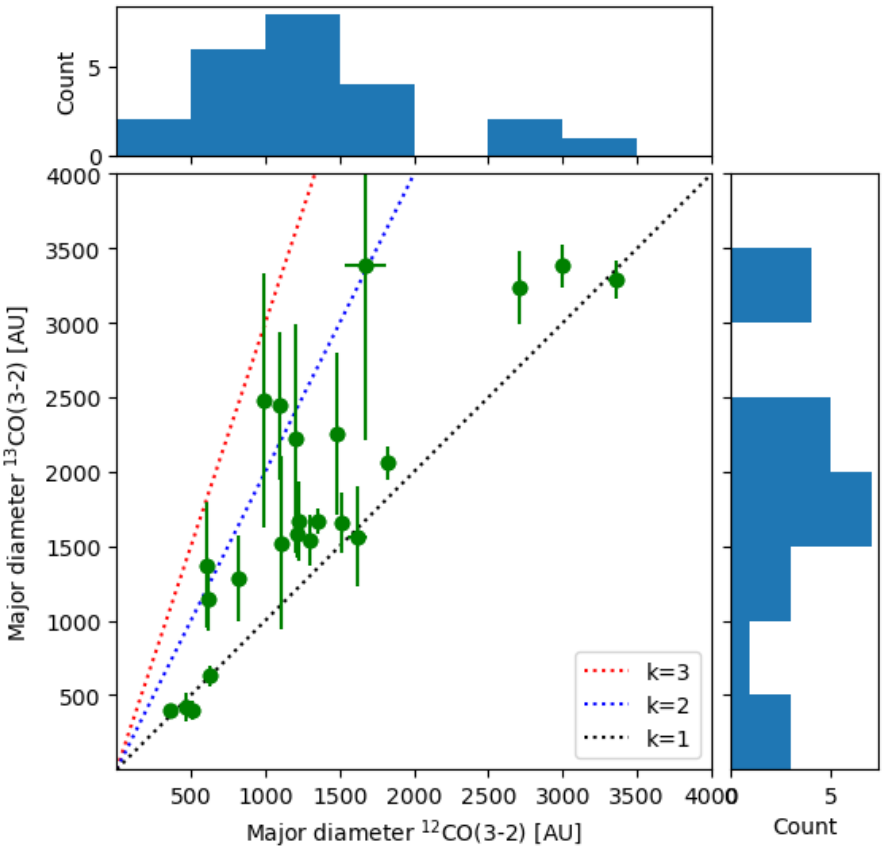

Figure 3.1: Diameter across the major axis of ^{13}CO$(3-2)$ envelopes plotted against diameter across major axis of ^{12}CO$(3-2)$ envelopes for 24 AGB stars. The top and right side show histograms counting the number of envelopes with sizes within 500 AU ranges. The dotted lines indicate slopes along which the size of the ^{13}CO$(3-2)$ emitting region is 1, 2, and 3 times larger.

3.2 Shapes of CO envelopes

To investigate the shape of the CO envelope, and how it varies between ^{12}CO and ^{13}CO we show the axes ratios for the 24 relevant sources in figure 3.2. The axis ratio is calculated by dividing the minor axis by the major axis and its value ranges between 0 and 1. An axis ratio of 1 translates to a perfectly spherical envelope, and a lower value means an increasingly elliptical distribution of gas. As a result the axis ratio works as a measure of how circular a source is, where values below 0.9 are considered non-spherical, in accordance with the discussion by Andriantsaralaza et al (2021) [3]. This limit is indicated by the dashed lines.

Figure 3.2 shows that a majority of stars have either a spherical ^{12}CO or ^{13}CO emission region. Only a few stars appear spherical in both isotopologues, and even fewer appear spherical in neither. The errors are significantly larger for ^{13}CO axis ratios, and overall very small for ^{12}CO axis ratios. To quantify the differences between the two axis ratios the weighted arithmetic mean was calculated for both

^{12}CO and ^{13}CO axis ratios respectively. The weighted arithmetic mean accounts for the inherent uncertainty of the data by weighting values with their associated error. Similarly one computes the standard error of the weighted mean. The weighted average ^{12}CO axis ratio was determined as 0.873 ± 0.003, and the weighted average ^{13}CO axis ratio as 0.883 ± 0.022. These weighted means are very comparable in size, showing that the general shapes of both emitting regions seem to match rather well over the entire sample. It is interesting that the mean axis ratio values are similar while few stars appear symmetric in both CO isotopologues.

One noticeable difference is the large standard error of the weighted mean for ^{13}CO ratios, which is about one order of magnitude larger than for ^{12}CO, indicating a larger spread of values. The large uncertainties of ^{13}CO axis ratios are also reflected in the figure. It should also be noted that the minimum value of the axis ratio during the fit was set to 0.5. The data points that have reached this value may not be trustworthy.

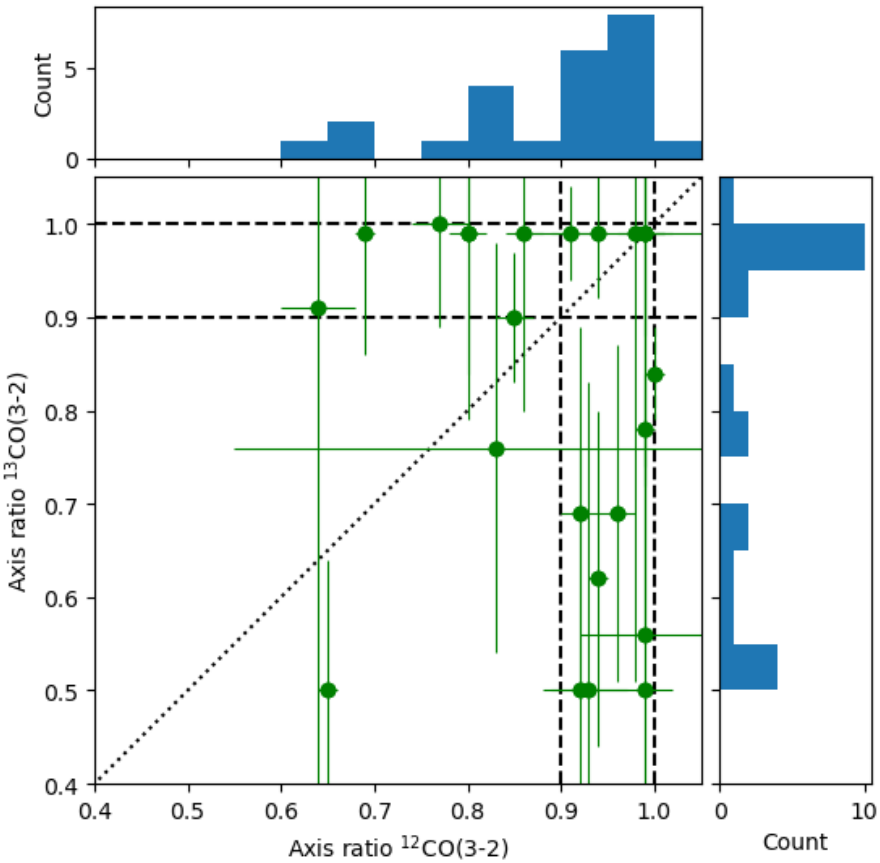

Figure 3.2: Axis ratios of the emitting regions of ^{12}CO$(3-2)$ and ^{13}CO$(3-2)$ plotted against one another for 24 AGB stars. The dashed lines mark the regions where emitting regions are considered spherical, and the dotted line marks where the two regions are similarly shaped. The figure also shows two histograms counting the number of stars in 0.05 ranges of axis ratios.

A naive interpretation of figure 3.2 might be that when one of the emission regions is spherically symmetric, the other most likely isn't. However with the large uncertainties in ^{13}CO axis ratios it is too early to tell that any such relation exists, especially when the overall mean matches so well between the two emission regions. Here it would be insightful to study the structure plots of individual stars in more detail to see if the structure between ^{12}CO gas and ^{13}CO gas differs.

3.3 Structures of individual stars

So far we've only presented general trends of the sample, taken at each star's systemic velocity. These quantities are useful for more sweeping statements, but miss details of the CSE. We now present structure plots of individual stars, showing how the four quantities major axis, minor axis, RA, and Dec of the emitting CO gas vary over different velocities. For the main discussion, graphs of a few select stars are presented and discussed in detail. A full collection of structure plots for all stars in the sample can be found in appendix A.

UY Cet

Figure 3.3 shows the structure in ^{12}CO and ^{13}CO for the star UY Cet, and was chosen to showcase the typical similarities between ^{12}CO and ^{13}CO structure. The error of the ^{13}CO major axis at the systemic velocity is $\sim$24% of its value. The error is also consistent throughout the entire velocity spectrum, except toward the edges. Naturally the signal-to-noise ratio decreases toward the edges, as the signal weakens toward more extreme doppler shifts. If we go too far on the velocity axis the emission completely vanishes and the algorithm tries to fit a 2D-gaussian to only noise. This explains why noise dominates toward the edges, and these values can be disregarded.

The general shape of the ^{13}CO major axis in the figure does not fluctuate and seems to follow the profile in ^{12}CO, indicating similar structures. The similarities include the gradual decline in major axis width toward the redshifted side, the large increase in noise and lack of a gradual drop toward the blueshifted side, the relatively constant axis width around the systemic velocity, and the position offset profiles. Physically this means that the centres and the general shapes seem to match for the two emitting regions. The major and minor axis lie around 4 arcseconds close to the systemic velocity for ^{13}CO, and only around 3 arcsec for ^{12}CO. This exemplifies the discussion of CO envelope sizes above, where we found ^{13}CO to be larger than ^{12}CO in general. For UY Cet the major axis values were determined as 3.30 ± 0.10 for ^{12}CO, and 5.03 ± 1.21 for ^{13}CO. The major and minor axis also seem to separate slightly more for ^{13}CO, lowering the axis ratio from 0.83 ± 0.28 for ^{12}CO to 0.76 ± 0.22. However these fluctuations are well within the uncertainties, making it impossible to tell whether this reduction in axis ratio is physical or coincidental.

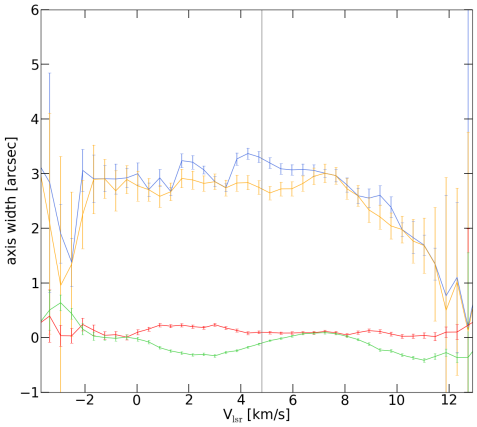

(a) Size and position of ^{12}CO(3-2) emission in UY Cet.

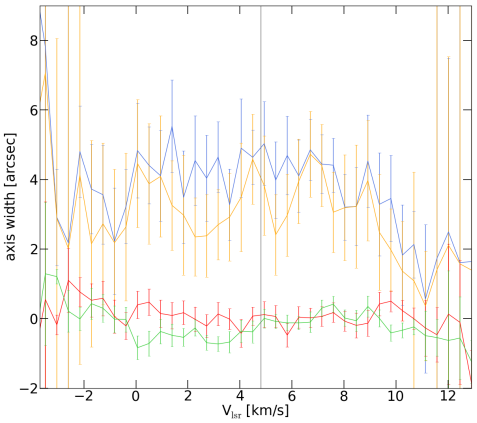

(b) Size and position of ^{13}CO(3-2) emission in UY Cet.

Figure 3.3: Structure plots of the star UY Cet. ^{13}CO has a lower signal-to-noise ratio but the general shapes seem to match. The blue line is the major axis of the emitting envelope, while yellow is minor axis. Red and green indicate the position offset in Right Ascension, and Declination, respectively. The grey vertical line down the centre indicates the systemic velocity of the star.

RZ Sgr

Next, we discuss the structure of the star RZ Sgr shown in figure 3.4. The figure shows some interesting features and also some striking differences between ^{12}CO and ^{13}CO. In ^{12}CO there is a prominent spike at $v \approx -32\,\mathrm{km/s}$, and also a large hump centred at around $v \approx -35\,\mathrm{km/s}$. The main difference between these two structures is that the spike corresponds to only one single channel, while the hump spans many channels.

The spike is very suspicious, and is difficult to explain from a physical perspective. It would seem that the CSE changes drastically for a certain velocity, to then return to its previous size in the next. At this specific channel the position of the emitting region completely changes. Furthermore the axis values more than double in size from around 3" to almost 7". Physically this makes no sense as the CSE cannot become more than twice as big and completely change position for just a single velocity just to reset in the next.

The spike is most likely the result of either a computational error or a noise spike. The LM algorithm used by uvmultifit is known to not always find the global minimum, but to always find a local minimum. As a result it is possible for the algorithm to get stuck if a poor initial condition is used. Secondly if another emission zone close to the star suddenly appears due to for example fluctuations in the noise, the algorithm might try to include both regions in the fit. This would place the centre somewhere in between as well as increase the size of the fitted envelope. However ^{12}CO emission generally has good signal-to-noise ratios. Fluctuations of the back-

ground are unlikely to reach high enough values to skew the emission region enough to double the size and change position so drastically.

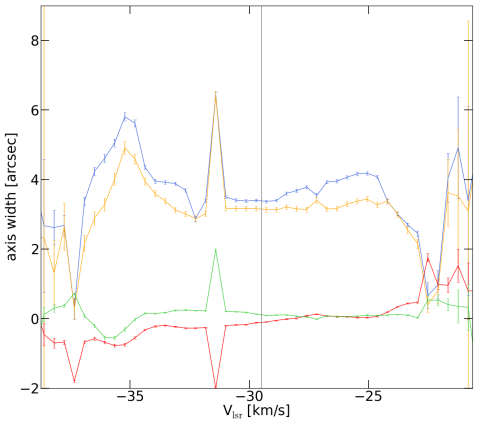

(a) Size and position of ^{12}CO(3-2) emission in RZ Sgr.

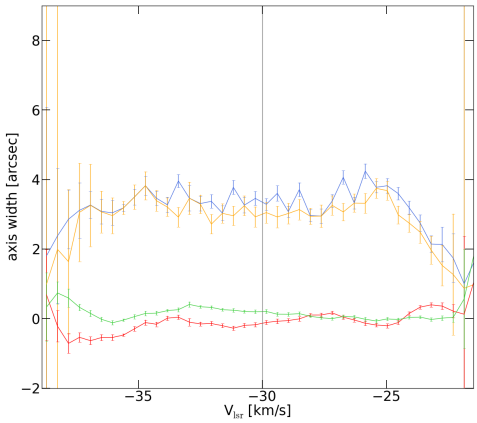

(b) Size and position of ^{13}CO(3-2) emission in RZ Sgr.

Figure 3.4: Structure plots of the star RZ Sgr. The ^{12}CO structure shows both a single-channel spike and a hump spanning many channels. These features are missing from the ^{13}CO structure.

The conclusion is that this single-channel spike is un-physical and the result of a faulty fit for this specific velocity. These spikes appeared occasionally in various stars during the fitting, and some further examples can be found in appendix A. Adjusting the initial conditions removed the spikes in many cases. As such it is most likely to be a computational error. Another version of the spike is a single-channel dip, where the size of the emitting region suddenly decreased. The same reasoning applies there, and it is most likely a computational error where the algorithm got stuck in a local minimum. An example of a star with prominent dips in the ^{12}CO structure is Y Pav, shown in figure 3.5.

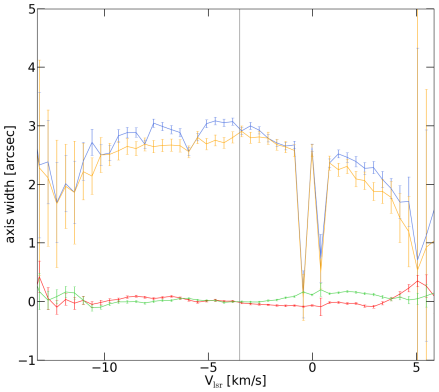

Figure 3.5: Structure plot of ^{12}CO for the star Y Pav, showing two prominent dips at velocities around $v = 0$.

Next we discuss the hump in figure 3.4, which covers many channels. Over the velocities of the hump the axis width increases and the centre position shifts gradually. This makes it unlikely to be a purely computational error, as it would mean the error is systematic over many data points. Interestingly the hump cannot be found in the ^{13}CO emission region at all, which instead stays stable. Similar humps appear in the structure plots for other stars as well, and it consistently appears only in the ^{12}CO spectrum, and never in the ^{13}CO spectrum. Examples of stars showing a hump in the ^{12}CO structure plot but not in ^{13}CO include CW Cnc, IRC-10529, IRC+10365, R For, R Hor, R Lep, R Vol, RV Aqr, RZ Sgr, T Mic, V821 Her, WX Psc. Structure plots of all these stars can be found in appendix A. Interestingly many of these stars have high mass-loss rates[2, 3].

One possible explanation for the hump is that it arises from the emission of another molecule rather than from the inherent structure of the CO gas. If the hump was due to an anisotropic distribution of CO gas, then it should appear in both ^{12}CO, ^{13}CO, and likely even other molecular lines of CO. In the first DEATHSTAR paper by Ramstedt et al.(2020) [2], similar humps were identified in the emitting regions of ^{12}CO(2-1). The molecular lines are separated by their frequency. It is therefore possible for another molecule to overlap with the ^{12}CO(3-2) spectrum without being visible close to other CO line emissions. While this could explain the presence of the hump in ^{12}CO(3-2) and not in ^{13}CO(3-2), it does not explain the presence of the humps reported for ^{12}CO(2-1) emission by Ramstedt et al. (2020). As a result, the hump being due to emission from another nearby molecular line is highly unlikely.

Since the hump appears in both ^{12}CO lines, but not for ^{13}CO, the explanation can likely be found in the different abundances of the isotopologues. In section 2.2, the basics of radiative transfer were explained. Most notably, RT effects are larger for more abundant gases and should impact the ^{12}CO emissions more than ^{13}CO. This could explain why no hump is seen in the ^{13}CO structure plot. Furthermore the hump should be more pronounced in stars with a high-density CSE.

Doppler effects shift the frequency of line emissions in the CSE. Since molecules absorb emission at the same frequencies that they emit, the chance of absorption is higher when the molecules travel in the same direction as the emissions. Molecules travelling at the same velocity experience no frequency shifts in relation to each other. However when the gas and emission travel in different directions, the relative frequency is shifted, and the emission is more likely to pass through the gas. As a result radiative transfer effects are more pronounced when coming from the gas travelling towards the observer, corresponding to the left side of the structure plots. This is in-line with our observations, where the hump always appears over the more negative velocities on the left side.

When radiation emitted close to the centre of high density ^{12}CO envelopes gets absorbed and remitted further out, the observer ends up seeing only the outermost layers. The effect is similar to what was discussed in relation to the larger perceived envelope sizes of ^{13}CO in section 3.1, where the ^{13}CO gas was explained to

be excited further out in the CSE, making the emitting region larger. As a result a substructure with increased major and minor axis could appear in the negatively doppler shifted region of the structure plot, forming a hump.

However, the peak major axis size being larger at the hump than the systemic velocity does not make much sense physically. The projected size should always be largest at the systemic velocity, and as such, the overly large axis sizes could be due to a computational error. For velocities where RT effects are strong, the emission profile could change, and might no longer be well approximated by a 2D-gaussian. For example the shape of the emission profile might become flatter or cut-off, due to the excited gas being distributed differently, as shown and briefly discussed in Ramstedt et al. (2020) [2]. When the algorithm tries to fit a 2D-gaussian to a differently shaped emission the resulting gaussian might be spread out, leading to an overestimated size of the emitting region. To investigate this further, imaged results showing the measured emission at the three velocities $\sim -24, \sim -29$, and ~ -35 are presented in figure 3.6. These images seem to indicate that the emission region at the velocity of the hump is smaller than at the systemic velocity, supporting the idea of the emission profile not being well represented by a 2D gaussian.

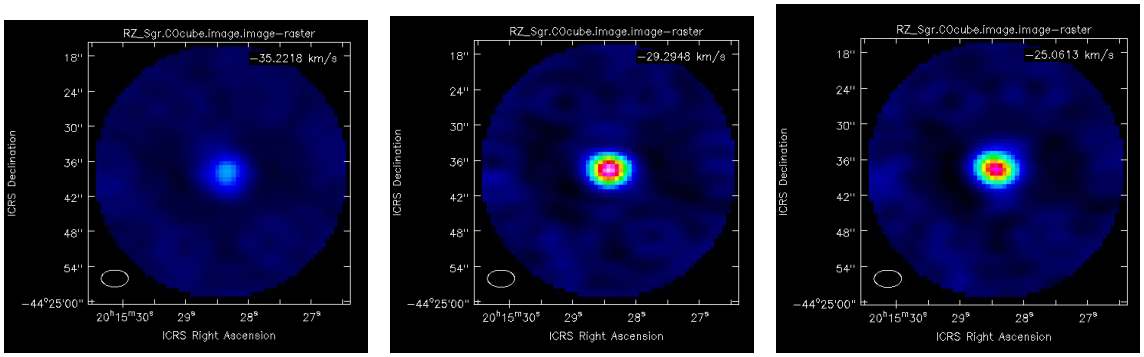

(a) v = -35 km/s **(b)** v = -29 km/s **(c)** v =-25 km/s

Figure 3.6: Images of the ^{12}CO(3-2) emitting region of RZ Sgr taken at three different velocities.

To summarise, the hump in figure 3.4 seems to be the result of a combination of factors. Firstly the asymmetrical effects of radiative transfer causes the hump to always appear on the left side of the structure plots. The radiative transfer effects are stronger for more dense gases, explaining why the hump is visible in ^{12}CO emission regions of high mass-loss stars, but not in ^{13}CO emissions. Lastly, by judging from the reconstructed images in figure 3.6, and from reasoning that the axis values should be largest at the systemic velocity, we suggest that the emission profile might deviate from a true gaussian due to the gas being excited differently. The algorithm still forces a gaussian fit onto a flatter, more cut-off distribution, leading to a wider emitting region in the structure plots.

Other than the hump and spike, an interesting feature of the ^{12}CO structure plot of RZ Sgr in figure 3.4 is the relationship between the minor axis and the major axis.

In previously presented structure plots, the values of these two variables fluctuated, making the actual shape hard to determine. In this ^{12}CO structure plot however, the minor axis is consistently smaller than the major axis, indicating that the shape is not perfectly spherical for any velocity. For ^{13}CO the difference is less pronounced. Lastly, the uncertainty in ^{13}CO is low compared to other presented stars such as UY Cet and TT Cen, making the reported values for size and shape of this star more reliable.

TT Cen

Figure 3.7 shows the structure plots of the star TT Cen in both ^{12}CO(3-2) and ^{13}CO(3-2). The structure plots of TT Cen were chosen to showcase how the emission region of a star that follows the standard CSE model is expected to look, and to showcase the limitations of noisy ^{13}CO data. Even though the ^{13}CO structure is noisy, the underlying shape seems to match that of the ^{12}CO emitting region. The sizes are still noticeably different.

The structure of ^{12}CO is almost perfectly symmetrical around the systemic velocity, corresponding to a star that closely follows the standard CSE model. The major axis peaks at the systemic velocity, then symmetrically decreases on both sides showing no substructures before fading into noise at the edges. The minor axis and major axis follow each other closely. As discussed above, the axis ratio works as a measure of the shape, and a consistent axis ratio close to one indicates a completely spherical distribution of gas. Furthermore the position offsets RA and Dec remain constant throughout the spectrum, meaning the centre of the emission region stays fixed. This is what an isotropic, spherically symmetric CSE is expected to look like. To summarise, we can judge from the graph that the CSE is spherical, isotropic and has a stable position. The ^{12}CO emitting region of TT Cen appears to follow the standard CSE model.

Compared to ^{12}CO, the structure of ^{13}CO in figure 3.7 is very noisy and neither position nor axis values are reliable. This was one of the stars excluded from the summarising figures because the major axis error exceeded 40% of its value. The structure plot verifies that the noise is consistent throughout the entire emission region, and that discarding this star from the summarising figures was valid. This highlights one of the limitations of the study, namely the occasionally very noisy ^{13}CO data.

At the same time however, the general shape of the ^{13}CO(3-2) emitting region appears to match that of ^{12}CO, suggesting that the underlying structure of ^{13}CO might be very similar to ^{12}CO in this case. Although due to the noise, a definitive claim is impossible to make. As a next step for future research one could look to improve the quality of some of the noisy ^{13}CO data by combining channels. Through this process one averages neighbouring channels of a data set. The goal of combining channels is to cancel some of the noise, which in turn increases the signal-to-noise ratio. This improves the stability of the data but sacrifices some of the resolution. Since 8 out of the 32 detected ^{13}CO emissions proved too noisy, the sample size could potentially be improved by 33% using this method.

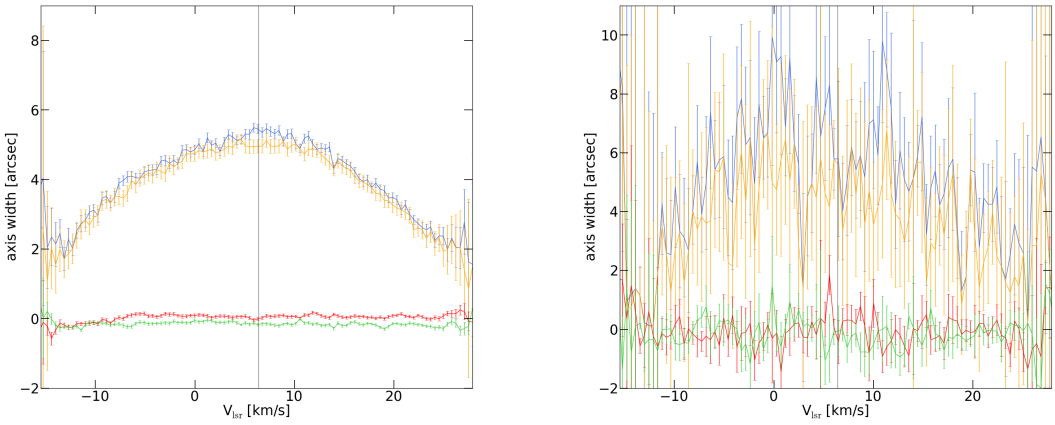

(a) ^{12}CO(3-2). **(b)** ^{13}CO(3-2).

Figure 3.7: Two structure plots showing size and position of emitting envelopes as a function of velocity for the star TT Cen. This star shows noisy ^{13}CO emission, and was excluded from the main sample. At the same time the underlying shape can be seen to match that for ^{12}CO.

4
Conclusion

This thesis project studied the CSEs of 61 AGB stars from the DEATHSTAR project with the goal of characterising the sizes and shapes of the ^{13}CO(3-2) emitting regions of those stars. To achieve this, line emission from ^{12}CO(3-2) and ^{13}CO(3-2) were investigated. Out of the 61 stars from the original sample, ^{13}CO emission was detected in 32. Using uvmultifit, 2D gaussians were fitted to the observed emissions for each velocity in their spectrums. ^{13}CO(3-2) emitting regions where found to be between 1 and 3 times as large as their ^{12}CO(3-2) counterparts. The larger size of ^{13}CO was in line with previous results from radiative transfer modelling, and could provide observational constraints, helping further improve these models. The shapes of the emitting regions were found to be very similar when considered over the entire sample, with an average axis ratio of 0.873 $\pm$0.003 for ^{12}CO, and 0.883 $\pm$0.022 for ^{13}CO.

To investigate this further, we looked deeper at the structure plots of a few individual stars, and discussed the limitations of summarising a star's structure using only fitting results at the systemic velocity, which fails to capture variations within the star itself. Furthermore, we showed some of the features that could appear in fits, such as spikes and humps. The spikes were concluded to be un-physical, and are believed to be a result of the LM-algorithm getting stuck in a local minimum during the fit. The humps, on the other hand are believed to be a combination of radiative transfer effect in dense circumstellar envelopes, which changes the emission profile, and resulting in an incorrect fit. The fact that the algorithm produces these problems highlights the importance of critically examining results of individual stars, rather than just the summarising features.

Out of the 32 stars showing ^{13}CO emissions, 8 were excluded due to high noise levels. For further research one could aim to improve the data quality of noisy ^{13}CO emissions through combining channels. This would improve sample size, and possibly result in lower uncertainties for ^{13}CO sizes and shapes at the cost of resolution.

To conclude, the sizes of ^{13}CO were found to be larger than those of ^{12}CO, in line with existing radiative transfer models. The shapes of the two envelopes were similar when the entire sample was considered, but deviated for individual stars. These deviations are attributed to the larger uncertainties of ^{13}CO data. The lower signal to noise ratio for ^{13}CO constitutes one of the limitations of the study. Still the reported values of size and shape for ^{13}CO envelopes can hopefully be used to constrain and improve mass-loss and radiative transfer models going forward.

Bibliography

[1] Andriantsaralaza, M. (2024) "Mass Loss of Evolved Stars, Improving Mass-Loss Rates and Distances", [Ph.D. thesis, Uppsala Univeristy].

[2] Ramstedt, S. Vlemmings, W.H.T., Doan,L., Danilovich, T. Lindqvist, M., Saberi, M., Olofsson, H., De Beck, E., Groenewegen, M. a. T., Höfner, S., Kastner, J. H., Kerschbaum, F., Khouri, T., Maercker, M., Montez, R., Quintana-Lacaci, G., Sahai, R., Tafoya, D., & Zijlstra, A (2020) DEATHSTAR: nearby AGB stars with the Atacama Compact Array. I. CO envelope sizes and asymmetries: A new hope for accurate mass-loss-rate estimates, *Astronomy & Astrophysics, 640*, A133. https://doi.org/10.1051/0004-6361/201936874

[3] Andriantsaralaza, M. Ramstedt, S. Vlemmings, W.H.T Danilovich, T. De Beck, E. Groenewegen, M.A.T. Höfner, S. Kerschbaum, F. Khouri, T. Lindqvist, M. Maercker, M. Olofsson, H. Quintana-Lacaci, G. Saberi, M. Sahai, R. and Zijlstra, A. "DEATHSTAR: nearby AGB stars with the Atacama Compact Array. II. CO envelope sizes and asymmetries: The S-type stars," *Astronomy & Astrophysics*, vol. 653, p.A53, Sep.2021.

[4] Busso, M., Gallino, R., & Wasserburg, G. J. (1999). Nucleosynthesis in asymptotic giant branch stars: Relevance for galactic enrichment and solar system formation. *Annual Review of Astronomy and Astrophysics*, 37(1), 239–309. https://doi.org/10.1146/annurev.astro.37.1.239

[5] Molaro, P., Aguado, D. S., Caffau, E., Prieto, C. A., Bonifacio, P., Hernández, J. I. G., Rebolo, R., Osorio, M. R. Z., Cristiani, S., Pepe, F., Santos, N. C., Alibert, Y., Cupani, G., Di Marcantonio, P., D'Odorico, V., Lovis, C., Martins, C. J. a. P., Milaković, D., Murphy, M. T., . . . Mascareño, A. S. (2023). The $^{12}C/^{13}C$ isotopic ratio at the dawn of chemical evolution. Astronomy and Astrophysics, 679, A72. https://doi.org/10.1051/0004-6361/202347676

[6] Keenan, P. C. (1954). Classification of the S-Type stars. *The Astrophysical Journal*, 120, 484. `https://doi.org/10.1086/145937`

[7] Habart, E., Walmsley, M., Verstraete, L., Cazaux, S., Maiolino, R., Cox, P., Boulanger, F., & Forêts, G. P. D. (2005). Molecular hydrogen. In Springer eBooks (pp. 71–91). `https://doi.org/10.1007/1-4020-3844-5_3`

[8] Cazzoli, G., Puzzarini, C., & Lapinov, A. V. (2004). Precise Laboratory Frequencies for the J ← J-1 (J=1, 2, 3, 4) Rotational Transitions of 13CO. *The Astrophysical Journal*, 611(1), 615–620. https://doi.org/10.1086/421992

[9] Varberg, T., & Evenson, K. (1993). Laser spectroscopy of carbon monoxide: a frequency reference for the far infrared. *IEEE Transactions on Instrumentation and Measurement*, 42(2), 412–414. https://doi.org/10.1109/19.278593

[10] Deathstar. [Online] (n.d.). `https://www.astro.uu.se/deathstar/`

[11] Choudhuri, A. R. (2010). *Astrophysics for physicists.* https://doi.org/10.1017/cbo9780511802218

[12] *ALMA Science Archive.* (n.d.). `https://almascience.nrao.edu/aq/`

[13] Muller, S. [European ALMA Regional Centre Network] (2021, Jan, 15) "I-TRAIN #3: UVMultiFit - Fitting visbility data with UVMultiFit" [Video]. YouTube. `https://www.youtube.com/watch?v=MlARlvc_ggM`

[14] Marti-Vidal, I. (2018), "UVMultiFit's Documentation" url: `https://mural.uv.es/imarvi/docums/uvmultifit/`

[15] Andriantsaralaza, M., Ramstedt, S., Vlemmings, W. H. T., & De Beck, E. (2022). Distance estimates for AGB stars from parallax measurements. *Astronomy and Astrophysics*, 667, A74. https://doi.org/10.1051/0004-6361/202243670

[16] Saberi, M., Olofsson, H., Vlemmings, W. H. T., De Beck, E., Khouri, T., & Ramstedt, S. (2020). CO and HCN isotopologue ratios in the outflows of AGB stars. *Astronomy and Astrophysics*, 638, A99. https://doi.org/10.1051/0004-6361/202037668

A

Structure Plots of Full Sample

Structure plots of entire sample listed in table 3.1 sorted alphabetically.

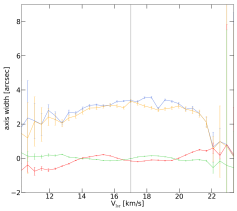

BK Vir 12CO(3-2).

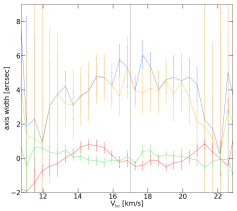

BK Vir 13CO(3-2).

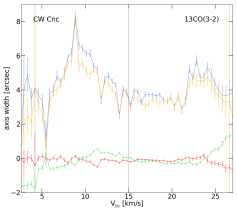

CW Cnc 12CO(3-2).

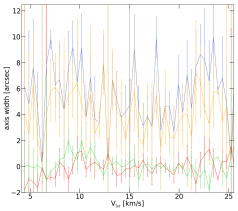

CW Cnc 13CO(3-2).

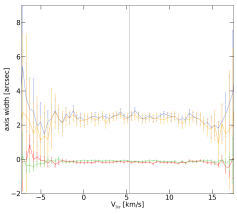

GI Lup 12CO(3-2).

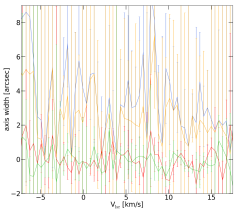

GI Lup 13CO(3-2).

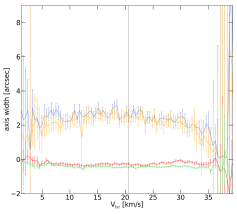

IRC-10401 12CO(3-2).

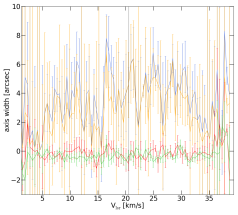

IRC-10401 13CO(3-2).

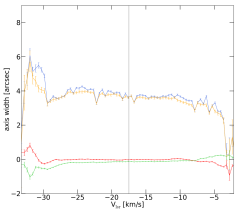

IRC-10529 12CO(3-2).

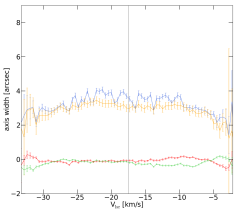

IRC-10529 13CO(3-2).

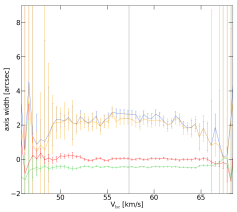

NSV 24833 12CO(3-2).

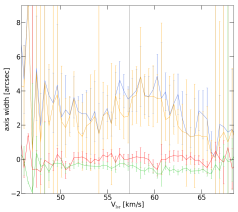

NSV 24833 13CO(3-2).

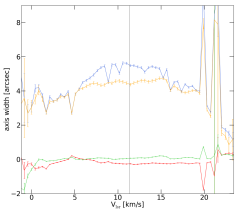

R Crt 12CO(3-2).

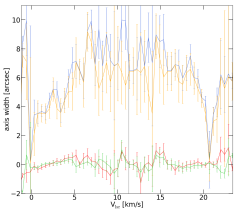

R Crt 13CO(3-2).

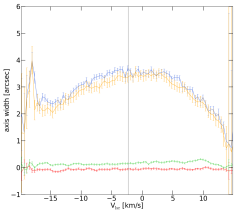

R For 12CO(3-2).

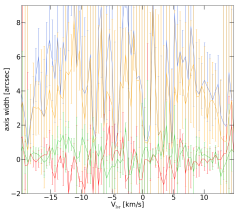

R For 13CO(3-2).

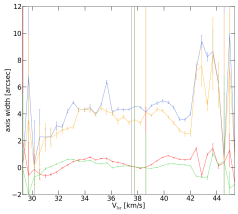

R Hor 12CO(3-2).

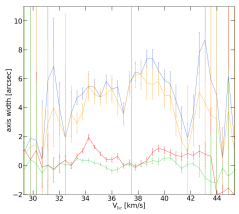

R Hor 13CO(3-2).

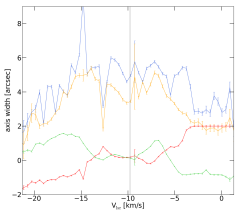

R Hya 12CO(3-2).

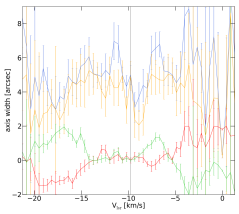

R Hya 13CO(3-2).

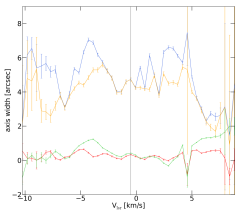

R Leo 12CO(3-2).

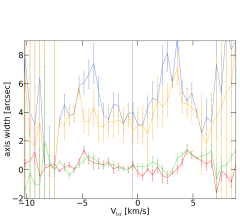

R Leo 13CO(3-2).

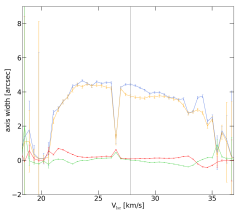

RR Aql 12CO(3-2).

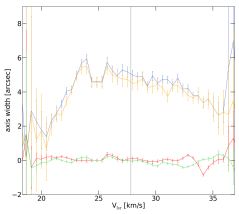

RR Aql 13CO(3-2).

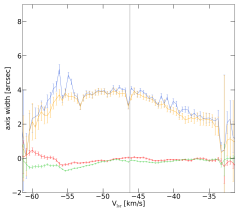

RT Sco 12CO(3-2).

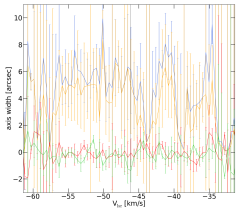

RT Sco 13CO(3-2).

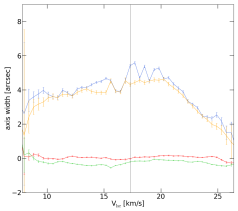

RT Vir 12CO(3-2).

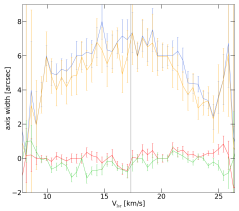

RT Vir 13CO(3-2).

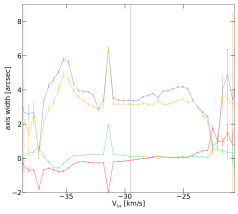

RZ Sgr 12CO(3-2).

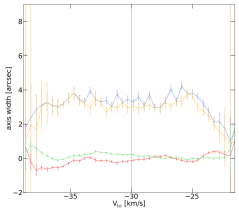

RZ Sgr 13CO(3-2).

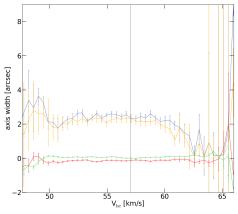

ST Sgr 12CO(3-2).

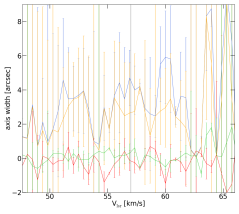

ST Sgr 13CO(3-2).

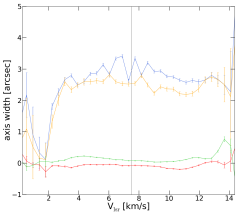

SU Vel 12CO(3-2).

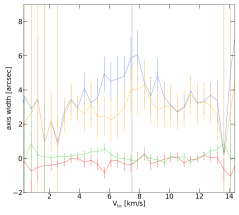

SU Vel 13CO(3-2).

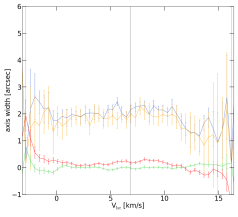

SV Aqr 12CO(3-2).

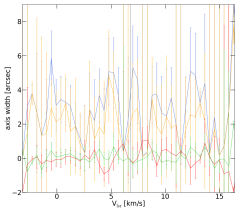

SV Aqr 13CO(3-2).

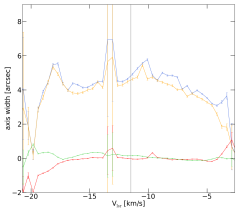

SW Vir 12CO(3-2).

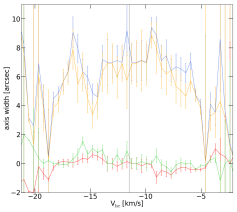

SW Vir 13CO(3-2).

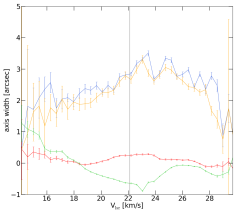

T Cet 12CO(3-2).

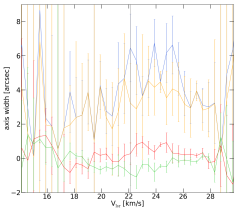

T Cet 13CO(3-2).

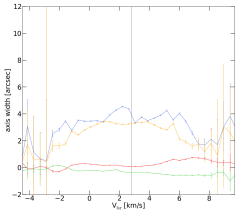

θ Aps 12CO(3-2).

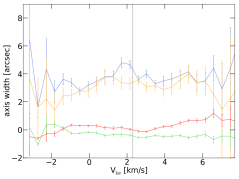

θ Aps 13CO(3-2).

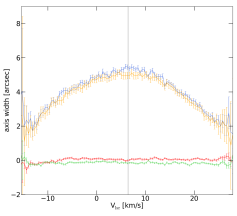

TT Cen 12CO(3-2).

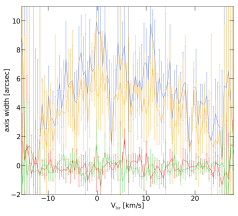

TT Cen 13CO(3-2).

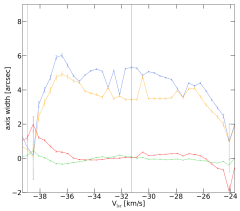

U Hya 12CO(3-2).

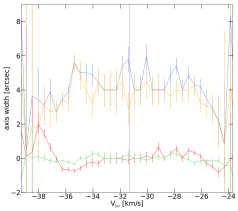

U Hya 13CO(3-2).

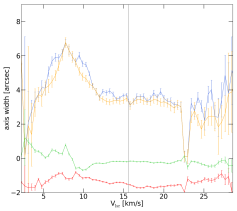

U Men 12CO(3-2).

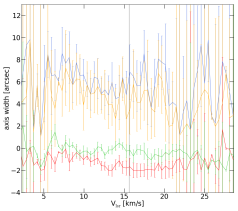

U Men 13CO(3-2).

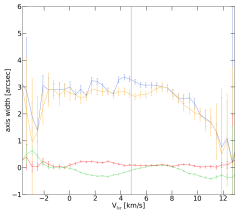

UY Cet 12CO(3-2).

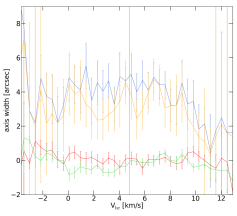

UY Cet 13CO(3-2).

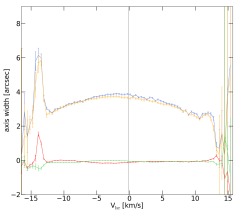

V821 Her 12CO(3-2).

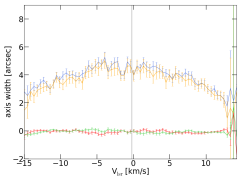

V821 Her 13CO(3-2).

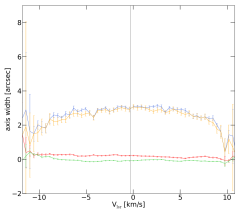

W CMa 12CO(3-2).

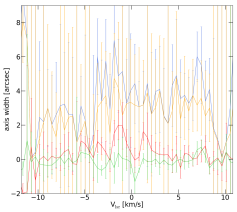

W CMa 13CO(3-2).

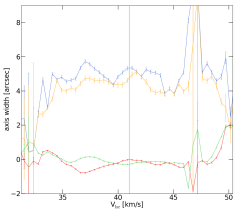

W Hya 12CO(3-2).

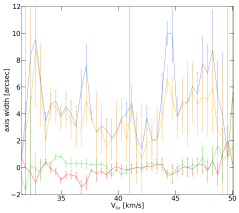

W Hya 13CO(3-2).

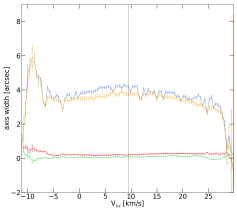

WX Psc 12CO(3-2).

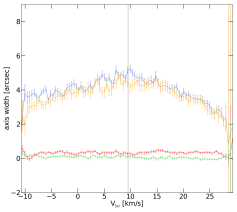

WX Psc 13CO(3-2).

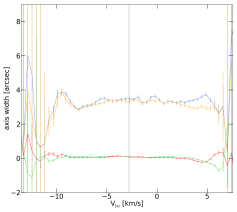

X TrA 12CO(3-2).

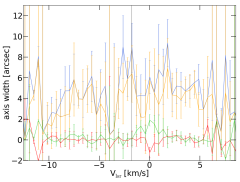

X TrA 13CO(3-2).

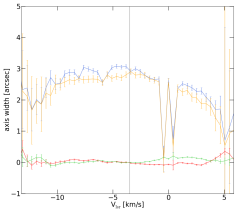

Y Pav 12CO(3-2).

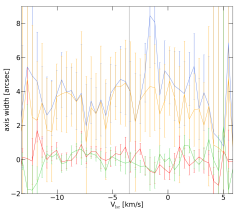

Y Pav 13CO(3-2).

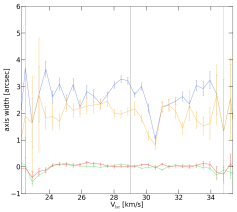

Y Scl 12CO(3-2).

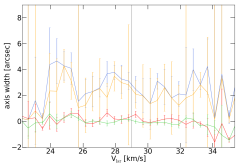

Y Scl 13CO(3-2).

DEPARTMENT OF PHYSICS
CHALMERS UNIVERSITY OF TECHNOLOGY
Gothenburg, Sweden
www.chalmers.se

CHALMERS
UNIVERSITY OF TECHNOLOGY